Marathon versus Sprint: Two Modes of Tropical Cyclone Rapid Intensification in a Global Convection-Permitting Simulation

FALKO JUDT[a], ROSIMAR RIOS-BERRIOS,[a] AND GEORGE H. BRYAN[a]

[a] National Center for Atmospheric Research, Boulder, Colorado

ABSTRACT: Tropical cyclones that intensify abruptly experience "rapid intensification." Rapid intensification remains a formidable forecast challenge, in part because the underlying science has not been settled. One way to reconcile the debates and inconsistencies in the literature is to presume that different forms (or modes) of rapid intensification exist. The present study provides evidence in support of this hypothesis by documenting two modes of rapid intensification in a global convection-permitting simulation and the HURDAT2 database. The "marathon mode" is characterized by a moderately paced and long-lived intensification period, whereas the "sprint mode" is characterized by explosive and short-lived intensification bursts. Differences between the modes were also found in initial vortex structure (well defined versus poorly defined), nature of intensification (symmetric versus asymmetric), and environmental conditions (weak shear versus strong shear). Collectively, these differences indicate that the two modes involve distinct intensification mechanisms. Recognizing the existence of multiple intensification modes may help to better understand and predict rapid intensification by, for example, explaining the lack of consensus in the literature, or by raising awareness that rapid intensification in strongly sheared cyclones is not just an exception to a rule, but a typical process.

SIGNIFICANCE STATEMENT: Hurricanes are serious threats to society—in particular those that suddenly and quickly intensify before striking land. Forecasting these "rapid intensification" events is a challenge, in part because we do not fully understand the science behind rapid intensification. This study furthers our understanding of hurricane rapid intensification by documenting that rapid intensification comes in different types. Specifically, we show that one type of rapid intensification happens under conditions that meteorologists have thought would lessen the chances of intensification. Awareness of such a type of rapid intensification could lead to better predictions of hurricane intensity because forecasters are more cognizant of this type of event and the conditions in which they occur.

1. Introduction

When a tropical cyclone (TC) experiences a period of intensification and its intensity increases by 30 kt (1 kt ≈ 0.51 m s^{-1}) or more over a 24-h interval, it is said to undergo "rapid intensification" (RI). RI is one of the most pressing challenges in tropical meteorology, not only because TCs that intensify quickly present a big problem for the public, but also because RI is notoriously difficult to predict. The prediction difficulties stem in part from a lack of scientific understanding. For example, there is no consensus on what processes cause RI or what conditions must be met for RI to happen. Scholars that study RI usually examine canonical RI events, that is, events where a weak, incipient TC enters a sustained period of RI and strengthens into a major hurricane (a "marathon" in the parlance of this paper). The present study documents that RI can also take on a "sprint" mode. We show that marathon and sprint modes have distinct underlying mechanisms, and we argue that the existence of multiple RI modes should be acknowledged for better understanding and predicting RI.

The idea that multiple modes of RI exist is not entirely new. In one of the earliest studies on RI, Holliday and Thompson (1979) partitioned western Pacific RI events into two types,

depending on whether the minimum pressure decreases steadily (type 1) or abruptly (type 2). Subsequent studies, however, did not develop this concept further, and the idea that multiple types of RI exist fell into oblivion.

Almost 40 years after Holliday and Thompson (1979), Ryglicki et al. (2018a) resurrected the idea that not all RI events are created equal. They classified RI events as either classical or atypical, where atypical RI events are those that occur in moderate vertical wind shear (atypical because moderate vertical wind shear is climatologically associated with weakening; Rios-Berrios and Torn 2017). The classical and atypical RI modes of Ryglicki et al. (2018a), however, neither seem to be congruent with the type 1 and 2 RI modes of Holliday and Thompson (1979), nor with two modes of RI that we document in this study.

Most RI-themed papers are agnostic about the issue of whether or not multiple types of RI exist. This is not a flaw in itself, but it could explain why the literature is lacking consensus on some aspects of RI. One prominent debate concerns the role of particularly vigorous convective cells, often called convective bursts. Some studies argue that convective bursts are triggers of RI (e.g., Guimond et al. 2010; Chen and Zhang 2013; Wang and Wang 2014), whereas other studies argue that there is no causal relationship between convective bursts and RI (e.g., Rogers 2010; Judt and Chen 2016). Some observational studies even imply a negative relationship between convective bursts and RI as symmetric rings of moderate convection are a more common precursor to

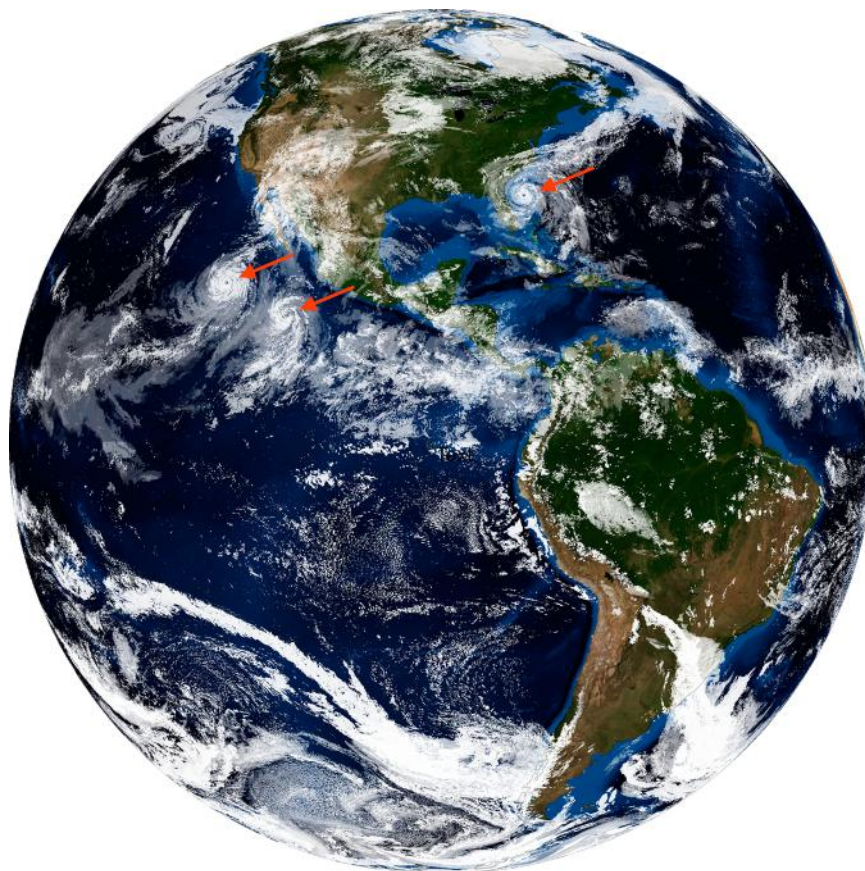*Corresponding author*: Falko Judt, fjudt@ucar.edu

FIG. 1. Simulated "full disk" satellite image from the global convection-permitting MPAS simulation used in this study. Three TCs are visible: two in the eastern Pacific and one in the Atlantic off the southeastern coast of the United States (red arrows).

RI compared to deep, asymmetric bursts (e.g., Kieper and Jiang 2012; Jiang and Ramirez 2013). The present study offers a solution for this debate by showing that convective bursts play a key role in one type of RI, but not in the other.

Another inconsistency in the literature involves vertical wind shear. Statistical studies clearly show that shear is unfavorable for RI (Kaplan and DeMaria 2003; Kaplan et al. 2010), but TCs in moderate shear often *do* experience RI (e.g., Rogers et al. 2015; Ryglicki et al. 2018a; Miyamoto and Nolan 2018; Rios-Berrios et al. 2018; Rios-Berrios 2020; Wang et al. 2022). In fact, even TCs that are impacted by strong shear are sometimes able to intensify rapidly (Molinari and Vollaro 2010; Nguyen and Molinari 2012). The present study, again, offers a solution for this inconsistency by proposing that shear is an unfavorable factor only in one mode of RI, but not in the other.

Besides providing an explanation for inconsistencies in the literature, the primary objective of the present study is to establish the presence of two distinct RI modes and to delineate their differences in intensity evolution, structure, and environmental characteristics. However, it is important to note that nature often defies rigid categorization, resulting in instances of crossover between these modes. Consequently, it is more appropriate to

view these modes as opposite ends of a spectrum, with frequent occurrences of overlap.

2. Data and methods

This study is based on a novel, yet unusual, dataset: a global convection-permitting simulation (Fig. 1). Global convection-permitting models (Satoh et al. 2019) offer the high resolution of regional models but lack some of their limitations, such as the need for lateral boundary conditions. Another TC-specific advantage of global simulations is that the TCs develop spontaneously and in full consistency with the model equations. In regional models, which have traditionally been used for high-resolution modeling studies of TCs, the initial vortex is usually sourced from a different model or prescribed, meaning that the vortex and model equations are initially inconsistent.

Global convection-permitting models do, however, have one major limitation: computational cost. Here, the computational cost limited us to a single 40-day simulation. The simulation was produced on the NCAR Cheyenne Supercomputer (Computational and Information Systems Laboratory 2019) and contributed to a model intercomparison project named the Dynamics of the Atmospheric general circulation Modeled On Non-hydrostatic Domains

TABLE 1. The set of parameterization schemes used in the MPAS simulation. If available, the WRF version from which the code was adapted is given.

Parameterization	Scheme	Reference
Convection	Scale-aware Tiedtke	Wang (2022)
Microphysics	Thompson (WRFv.3.8.1)	Thompson et al. (2008)
Land surface	Noah	Niu et al. (2011); Yang et al. (2011)
Boundary layer	MYNN (WRFv.3.6.1)	Nakanishi and Niino (2006, 2009)
Surface layer	MYNN (WRFv.3.6.1)	Nakanishi and Niino (2006, 2009)
Radiation, LW	RRTMG	Iacono et al. (2008)
Radiation, SW	RRTMG	Iacono et al. (2008)
Cloud fraction for radiation	Xu–Randall	Xu and Randall (1996)
Gravity wave drag for orography	YSU (WRFv.3.6.1)	Hong et al. (2008)

(DYAMOND; Stevens et al. 2019). As such, the simulation was not specifically designed for studying TCs. This may seem to be a disadvantage, but it turned out to be an asset: we had no control over the TCs that developed during the 40-day simulation, and so our sample of TCs is much less affected by selection bias than traditional high-resolution modeling studies. In fact, we believe that the findings of this study only came to be because we were dealt a global, quasi-random, high-resolution sample of TCs.

a. Simulation setup

The simulation was produced with the Model for Prediction Across Scales-Atmosphere (MPAS-A), a nonhydrostatic atmosphere model designed for weather and climate applications (https://mpas-dev.github.io; Skamarock et al. 2012). The model was set up on a quasi-uniform mesh with 3.75 km mean cell spacing and 75 vertical levels. Following the DYAMOND protocol (Stevens et al. 2019), we initialized the model with the European Centre for Medium-Range Weather Forecasts (ECMWF) analysis valid at 0000 UTC 1 August 2016 and integrated it for 40 days (1 August–10 September 2016), using a time step of 20 s. The sea surface temperature and sea ice fields were prescribed with 7-day running-mean analyses from ECMWF. In other words, there was no interactive ocean.

The parameterization schemes used for approximating subgrid-scale processes are listed in Table 1. These schemes were adapted from the WRF Model and are generally well-known in the mesoscale modeling community. One exception is the recently developed scale-aware Tiedtke cumulus parameterization scheme (Wang 2022). We used this scheme because a grid size of 3.75 km is in the convective "gray zone," i.e., convection is only partially resolved, and some form of cumulus parameterization may still be beneficial (e.g., Freitas et al. 2020; Becker et al. 2021). In this particular simulation, the convection scheme produced about 10% of the of total tropical precipitation (Judt and Rios-Berrios 2021).

TC-relevant fields such as 10-m wind, sea level pressure, radar reflectivity, etc., were written to disk at 15-min intervals. This relatively high frequency prevents under-sampling of the intensification process and allows us to capture the life cycle of phenomena with short time scales, such as convective bursts.

b. TC tracking and RI identification

The TC tracking method we used is the same as in Judt et al. (2021) and consists of three steps:

1) Interpolate the model fields from the native 3.75-km mesh to a regular latitude–longitude grid with 0.5° resolution.
2) Run the GFDL vortex tracker (Biswas et al. 2018; Marchok 2021) in *genesis mode* on the 0.5° grid. The tracker searches for TCs and writes track files that contain center location (latitude, longitude), maximum wind speed (v_{max}), and minimum sea level pressure (p_{min}) at 15-min intervals. Note that the track files contain information from the interpolated (i.e., coarsened) data.
3) Use the TC center information from step 2 to search for the actual v_{max} and p_{min} in the original high-resolution model output files, and overwrite the data in the track files with these new values. Run the iterative center-finding algorithm of Nguyen et al. (2014) on the high-resolution mesh files and use the obtained latitude and longitude values to overwrite the original values in the track files.

The simulation produced 23 TCs whose intensity and structure was deemed realistic (Judt et al. 2021). Seven of those 23 TCs, i.e., roughly one out of three, experienced RI. We obtained this number by applying the "30 kt in 24 h" RI criterion to a downsampled (i.e., smoothed) version of the original noisy 15-min v_{max} data. Specifically, we used the *pandas.DataFrame.resample()* method from the Python pandas library to reduce the sample rate from 15 min to 6 h. As a result of this smoothing operation, the model-derived intensities are more consistent with the 6-hourly v_{max} analyses in the "best tracks" (Landsea and Franklin 2013). This consistency helps to contextualize this work into the existing literature because the best tracks are not only the main data source for identifying RI in real storms, but also for the definition of RI itself (Kaplan and DeMaria 2003).

Aside from identifying RI cases, we also used the downsampled data to define RI onset. RI onset is simply the time of first occurrence after which the downsampled v_{max} increases by at least 30 kt over the following 24 h. Note that this definition of RI onset does not always conform with the subjective notion of RI onset. (By "subjective notion of RI onset" we mean the time of greatest increase in the intensification rate.)

Finally, we acknowledge that the 40-day time span of our simulation reaches well beyond the predictability limit of day-to-day weather (Judt 2018; Zhang et al. 2019). The simulation is therefore not expected to capture the storms that occurred in reality, nor do we expect that the simulated storms have real world counterparts. Hence, the simulated
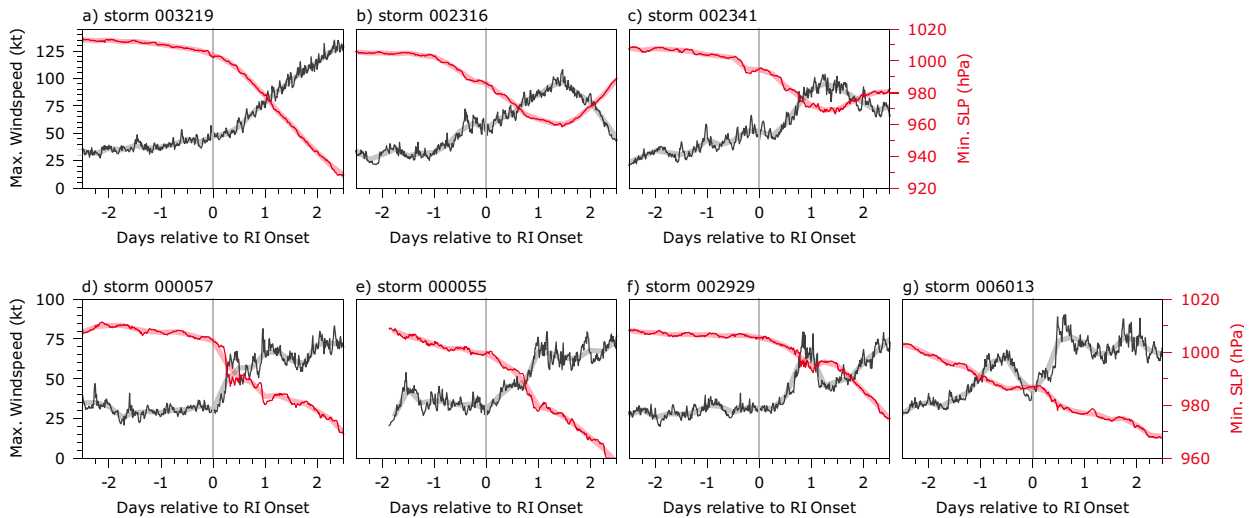
FIG. 2. Time series of v_{max} (black) and p_{min} (red) of the seven RI cases. The 15-min data are plotted in thin lines; the 6-hourly downsampled data are plotted in thicker translucent lines in the background. Note the different y-axis limits in (d)–(g) vs (a)–(c).

TCs are identified by a six-digit number, not by name (e.g., storm 003219).

3. Overview of RI cases and separation into marathon and sprint events

Time series of v_{max} and p_{min} provide an overview of the seven RI cases (Fig. 2). For easier referencing, the time series are centered on RI onset. In all seven cases, RI began when the TCs were of or just below tropical storm intensity (v_{max} between 30 and 54 kt). Five of the seven RI cases occurred in the western Pacific (storms 000055, 000057, 002929, 002316, and 006013), and one case occurred in each the eastern Pacific and Atlantic (storms 002341 and 003219, respectively).

The deliberate arrangement of Fig. 2 reflects the broad classification of the seven RI cases into two distinct groups. The cases in the top row, Figs. 2a–c, exhibit a moderately paced and prolonged period of intensification. On the other hand, the cases in the bottom row, Figs. 2d–g, display explosive and short-lived bursts of intensification. These contrasting characteristics—moderately paced and long-lasting versus explosive and short-lived—reminded us of track and field athletics and its diametric disciplines of marathon and sprint. And just as a marathon covers a longer distance than a sprint, the marathon cases reach a higher peak intensity than the sprint cases. More specifically, all three marathon RI cases reach major hurricane status (category 3+), whereas the four sprint cases only reach category-1 or -2 intensity.

Marathon and sprint RI cases not only differ in intensity evolution, but also in vortex strength and vortex structure (Fig. 3). At the time of RI onset, the vortices of the marathon-mode cases, are comparatively small, symmetric, and have well-defined centers in wind and pressure (Figs. 3a–c). In contrast, the vortices of the sprint-mode cases are large, asymmetric, and have poorly defined centers (Figs. 3d–g). In fact, "gyre" may be a more apt term than "vortex" when referring to these sprawling systems.

Besides being overall less organized, the sprint cases are also weaker than the marathon cases. More specifically, the maximum surface winds in three of the four sprint cases are only in the 10–15 m s^{-1} range (Figs. 3d–f), whereas the marathon cases have wind speeds $\geq$ 20 m s^{-1} (Figs. 3a–c). Storm 006013 is an outlier in the group of sprint cases and is as strong as the marathon cases, yet its structure is more similar to the other sprint cases (Fig. 3g).

In summary, there are fundamental differences in intensification and vortex structure between the marathon and sprint cases. However, it is important to reiterate that there is some crossover between the two groups, and not all cases fit neatly into one category. For instance, storm 002341 (Fig. 2c) does not align perfectly with the previous two marathon cases, but it also lacks the explosive intensification burst of the sprint cases. Despite the presence of crossover cases, the distinctions between marathon and sprint RI cases indicate that the two modes represent distinct intensification mechanisms. The following sections will present more evidence in support of this hypothesis, beginning with a more in-depth documentation of the differences in intensity evolution.

4. Differences between marathon and sprint RI modes in intensification, structure, and mechanisms

To highlight the differences between the two RI modes in more detail, we cross-examine the archetypes of each mode, i.e., the two cases that best embody each mode's characteristics. Specifically, we use storm 003219 to represent the marathon mode (Fig. 4a) and storm 000057 to represent the sprint mode (Fig. 4b).

The cross-examination exposes a number of contrasts, such as

- a main intensification period that is long-lasting (marathon mode) versus one that is short-lived (sprint mode),
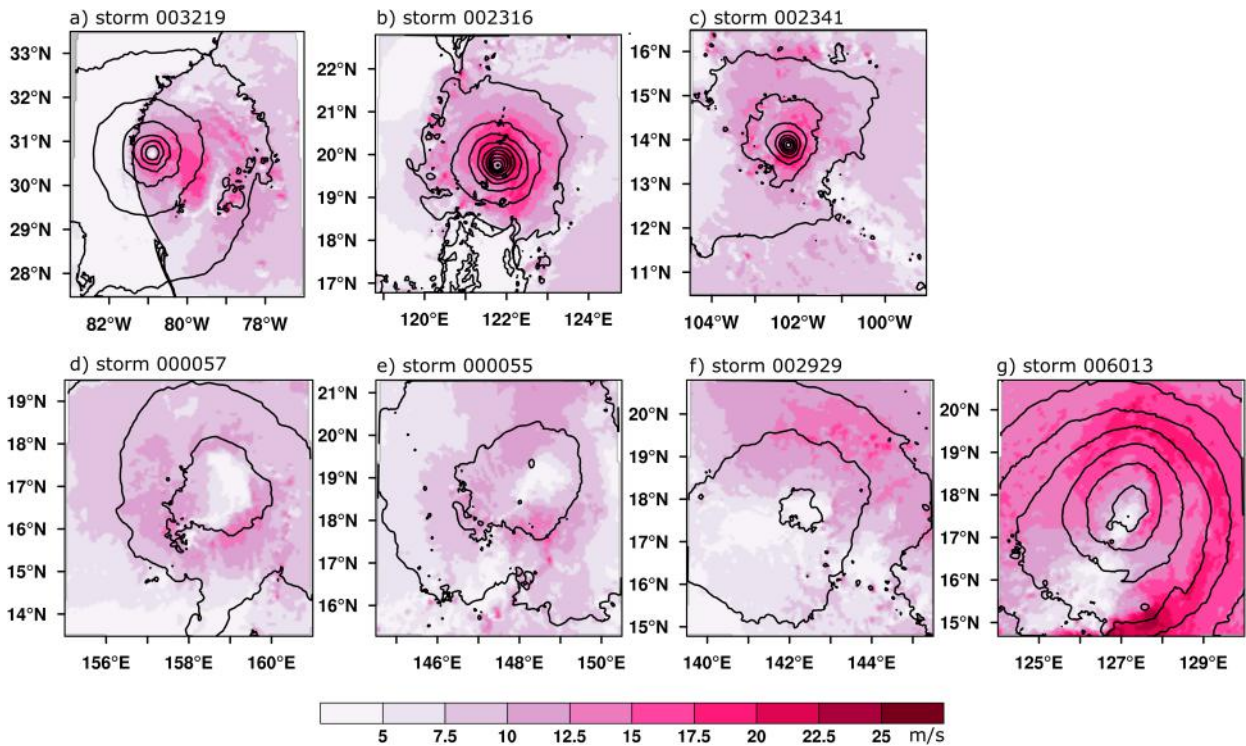
FIG. 3. Snapshots of surface wind (color shading) and sea level pressure (contours; every 2 hPa) of the seven RI cases at RI onset.

- an intensification rate during RI that is quasi-constant (marathon mode) versus one that is wildly fluctuating (sprint mode), and
- a transition from pre-RI to RI phase that is smooth and continuous (marathon mode) versus one that is practically discontinuous (sprint mode).

Overall, the intensity evolution of the marathon RI archetype in Fig. 4a resembles that of a canonical RI event and follows the three stage intensification model of Miyamoto and Takemi (2013) (the three stages are slow intensification, RI, steady state). In particular, the uninterrupted 2.5-day-long RI phase spans the evolution from tropical storm ($v_{max} = 47$ kt,
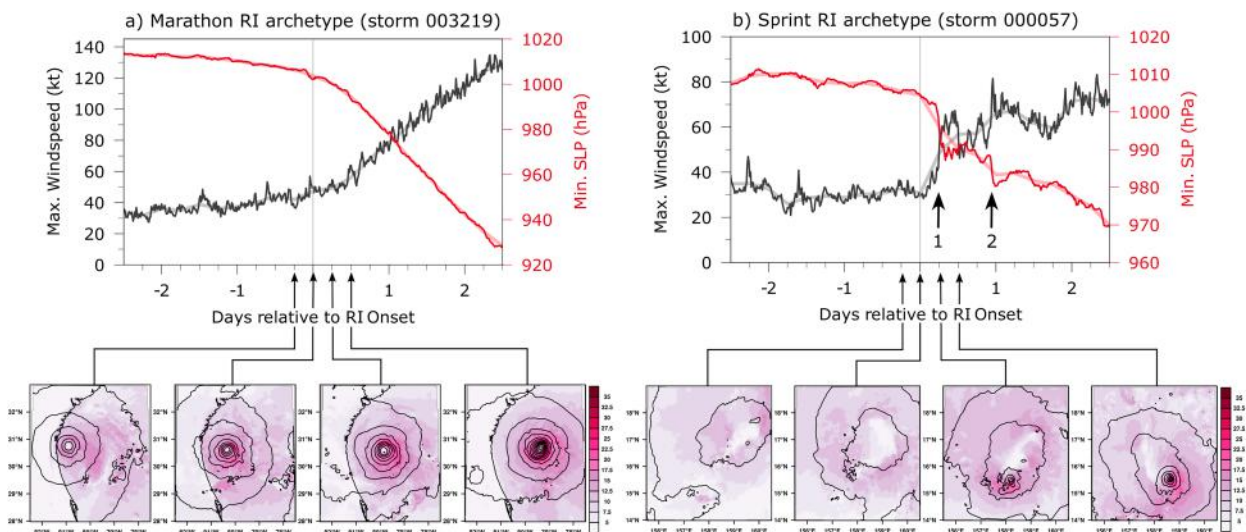

FIG. 4. Comparison of (a) marathon mode archetype and (b) sprint mode archetype. The time series show v_{max} (black) and p_{min} (red) as in Figs. 2a and 2d. The panels below the time series show plan views of surface wind (color shading; in m s^{-1}) and sea level pressure (contours; every 2 hPa) at the indicated times. The arrows in (b) point to the primary and secondary intensification burst. Note the different y-axis limits.

$p_{\min}$ = 1003 hPa) to high-end category-4 hurricane ($v_{\max}$ = 135 kt, $p_{\min}$ = 921 hPa; Fig. 4a). To a good approximation, both $v_{\max}$ and $p_{\min}$ are linearly increasing and decreasing, respectively, during the RI phase.

The intensification of the sprint RI archetype, on the other hand, does not follow the canonical picture of RI (Fig. 4b). The intensification is anything but linear and, in fact, resembles a step function. More specifically, virtually all of the intensification happens in two discrete bursts (marked by "1" and "2" in Fig. 4b). The primary intensification burst occurred 6 h after RI onset and caused an increase in $v_{\max}$ from 36 to 65 kt within 3 h alongside a drop in $p_{\min}$ from 1002 to 987 hPa. Subsequently, the storm entered a roughly 12-h-long quasi-steady-state period, as indicated by the horizontal trend in pressure (there were substantial fluctuations in wind speed during this period, but again, without a clear trend). A secondary, less intense burst occurred near the 1-day mark after RI onset and caused $v_{\max}$ to increase from 60 to 81 kt and $p_{\min}$ to drop from 988 to 982 hPa within 45 min. From the onset of the first burst until the conclusion of the second burst, the TC only intensified from a tropical storm ($v_{\max}$ = 36 kt) to category-1 hurricane ($v_{\max}$ = 81 kt).

As for the evolution of vortex structure, the marathon case exhibits a classic "spinup of a weak vortex" pattern (Fig. 4a, plan views). The sequence starts 6 h before RI onset with a weak but well-defined vortex. Even at this early time, the vortex has a symmetric core and a broad annulus of stronger winds surrounding a calm center.[1] Aside from developing a more pronounced eyewall, the overall structure does not change significantly during the transition from pre-RI to RI period, and the vortex maintains its symmetric structure while pulling away from land and strengthening at an increasing rate.

The evolution of vortex structure in the sprint RI case does not depict a classic spinup process. Rather, the sprint case shows a sudden development of a new center within the broader "parent circulation" (Fig. 4b, plan views). The sequence starts with the sprawling, asymmetric parent circulation, here easiest to recognize as a broad depression in the surface pressure field. Around RI onset, the structure is largely the same, although there are signs of noise in the pressure field to the southwest of the broad center. At RI onset +6 h, concurring with the primary intensification burst, a mesovortex has appeared in the wind and pressure fields. The mesovortex broadens over the next 6 h, and evolves into a small TC (diameter < 100 km) that moves counterclockwise within the background flow of the much larger parent circulation (diameter > 1000 km).

The fact that intensification burst and mesovortex happen at the same time is no coincidence. In fact, the intensification burst is a manifestation of the sudden development of the mesovortex and its subsequent spinup into a "true" TC. In other words, the mesovortex-turned-TC is the proximate cause of RI in the sprint RI archetype. For a more detailed

view of this dynamic process, we present hourly snapshots of winds and sea level pressure (Figs. 5a–c), vertical wind and geopotential height at 700 hPa (Figs. 5d–f), and simulated radar reflectivity (Figs. 5g–i).

The 3-h sequence of plots visualizes the prominent roles of vigorous asymmetric convection and the previously introduced mesovortex in this RI event. The sequence begins at RI onset +5 h and shows a vigorous convective burst located on the southwestern portion of the sprawling circulation (Fig. 5, left column). The burst consists of multiple strong up- and downdrafts with extreme gridcell values of +11 and −4 m s^{-1}, respectively (Fig. 5d). It seems that the low-level flow accelerates into the convecting mass, and the strongest winds of the entire system, 20 m s^{-1}, are located on the radially outward side of the burst (Fig. 5a).

Only 1 h later, the mesovortex had developed at the downwind end of the convective burst (Fig. 5, center column). The vortex, measuring roughly 50 km across, is readily identified by the circular isolines in sea level pressure and 700-hPa geopotential height (Figs. 5b,e). The vertical motion field still consists of individual convective-scale up- and downdrafts, now with extreme values of +18 and −5 m s^{-1} (Fig. 5e). Upward motion seems to be predominant in the vortex itself, but downward motion does exist in its outer regions. The reflectivity field seems to have coalesced into a slightly more coherent shape, and the strongest reflectivity values are either directly associated with the mesovortex or very close nearby (Fig. 5h).

The mesovortex intensified over the following hour and started to separate from the area of strongest convective overturning (Fig. 5, right column). The intensification of the vortex is manifested by the tighter spacing of the isobars and isohypses in Figs. 5c and 5f; the wind speed increased too, but this is hard to see in Fig. 5c because of the densely packed isobars. As a consequence of pulling away from the strongest convection, the vertical motion inside the vortex is not as strong as previously, and downward motion now takes up half of the circulation. Accordingly, the strongest reflectivity is now somewhat separated from the vortex (Fig. 5i).

In the hours that follow the initial mesovortex development shown in Fig. 5, the mesovortex grows in scale and "absorbs" the parent vortex (Fig. 6). A consequence of this process is that the clear distinction between small-scale mesovortex and large-scale parent circulation vanishes. At RI onset +22 h, the merger process has concluded and all that is left is a typical TC-size vortex without a sign of the original features of two distinct scales (Fig. 6c). Shortly after the snapshot in Fig. 6c, the second intensification burst occurs (arrow labeled "2" in Fig. 4). This intensification burst is also associated with a convective burst, but at this time, the convective burst does not produce a mesovortex and there is no center reformation (likely because the vortex is better defined than the original parent circulation and more resistant to perturbations). Rather, the convective burst "pulls" the surface centers toward the area where maximum heating occurs, which led to a briefly asymmetric structure of the vortex before subsequent axisymmetrization (not shown).

In summary, the RI process in the marathon case embodies a classical TC spinup event. The sprint RI case, on the other hand, is intimately related to the birth of a mesovortex, its initial intensification, and subsequent growth though absorption

---

[1] The outer wind field is asymmetric because the storm is close to land and friction reduces the wind speed over the western half of the outer circulation.
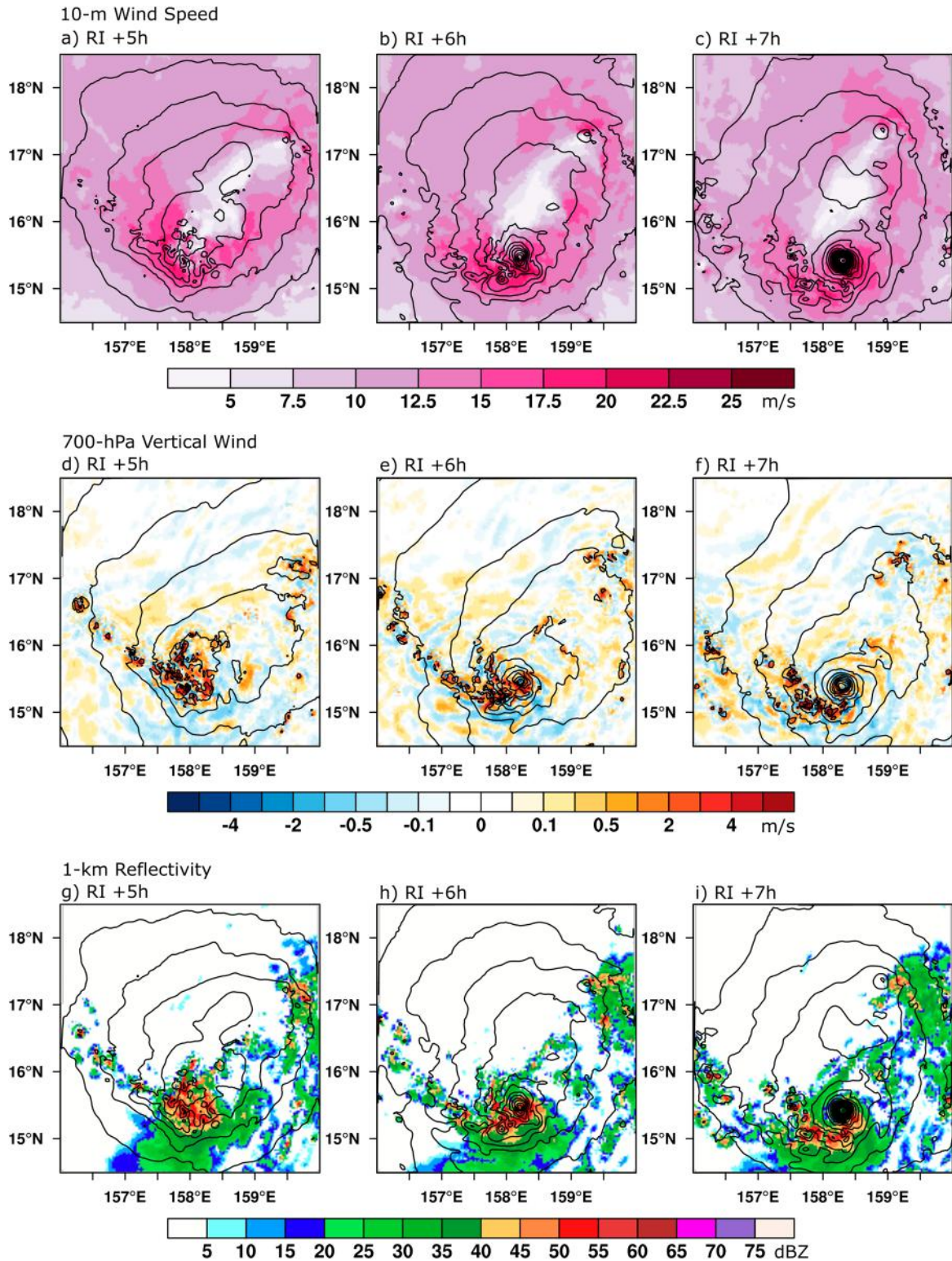
FIG. 5. Development of the mesovortex in the sprint-mode archetype as displayed by (a)–(c) surface wind (color shading) and sea level pressure (contours), (d)–(f) 700-hPa vertical wind (color shading) and geopotential height (contours; every 10 m), and (g)–(i) 1-km simulated radar reflectivity (color shading) and sea level pressure (contours; every 1 hPa). (left) Valid at RI onset + 5 h, (center) valid at RI onset + 6 h, and (right) valid at RI onset + 7 h.
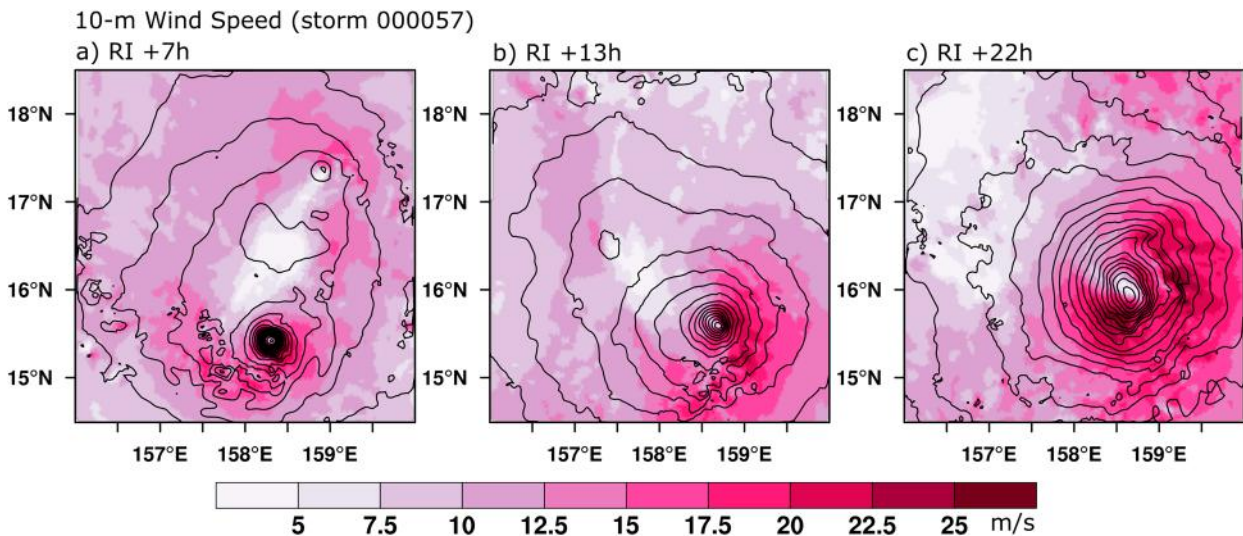
FIG. 6. Growth of the mesovortex and its merger with the parent circulation, as depicted by snapshots of surface wind (color shading) and sea level pressure (contours; every 1 hPa). Times relative to RI onset are indicated above each panel.

of the parent circulation. In the following subsection, we will investigate the differences in structure evolution in more detail.

a. Azimuthally averaged wind profiles

Radial profiles of azimuthally averaged tangential wind ("wind profiles" for short) are often used to study the inner workings of a TC. For example, wind profiles are helpful in understanding the fundamental relationship between storm structure and intensification (e.g., Stern et al. 2015; Li et al. 2021; Wu and Ruan 2021). Here, we will use wind profiles to examine the evolution of the vortex structure from 24 h before to 24 h after RI onset. Specifically, we want to answer the questions of whether RI is preceded by the formation of a well-defined RMW wind as implied by Miyamoto and Takemi (2013, 2015).

The wind profile evolution of the two archetypes is displayed in Fig. 7. Each profile represents a 6-h time average ending at the color-indicated time. The differences between the marathon RI mode (Fig. 7a) and the sprint RI mode (Fig. 7b) are striking, albeit not unexpected given the differences in vortex structure already depicted in the plan views of Fig. 4.

The "upward" progression of the wind profiles in Fig. 7a illustrates the continuous amplification of the primary vortex, one of the hallmarks of the marathon RI mode. The individual wind profiles are approximately self-similar, indicating that no major structure changes besides intensification and growth occur. The profiles from RI onset −24 h up to RI onset evolve slowly, in agreement with the slow intensification before RI seen in Fig. 4a, but the pace quickens after RI begins. In particular, the profiles from RI onset +12 h and later resemble those of a canonical TC in that the tangential wind increases rapidly as one moves radially outward from the center to the RMW and falls off again in an approximate $1/r^{0.3}$ fashion for radii greater than the RMW.

In support of Miyamoto and Takemi (2013, 2015), an RMW is already present before RI begins. Even the profile that represents the 6-h period ending one day before RI onset (dark purple) depicts a broad but noticeable peak near 50-km radius. Between 24 and 12 h before RI, the RMW shifts inward from 50 to about 30 km. There is no clear sign of a further contraction, however, and the RMW remains near 30-km radius from 12 h before RI all the way throughout RI. The fact that contraction ceases while the storm still intensifies agrees with the findings of Stern et al. (2015) and Li et al. (2021).

The wind profile evolution in the sprint RI case reveals a major restructuring event around RI onset. Prior to RI, the profiles are flat and the tangential wind gently increases out to about 100-km radius beyond which it remains constant. The peak magnitude of the azimuthally averaged tangential wind is less than 8 m s^{-1}, a low value for a TC. Perhaps most importantly, there is no indication of an RMW at any point before RI begins. While the overall flat structure does not change much until RI begins (RI + 6 h represents the 6-h period from RI onset to RI onset + 6 h), changes are all the more drastic after RI onset. The flat wind profile transitions to a peaked one within a few hours, and a clear RMW around 15–20-km radius becomes evident. This fast-paced transition is a manifestation of the center reformation caused by the mesovortex. In agreement with the quasi–steady state that the storm entered following the primary intensification burst (Fig. 4b), the peak value of the wind profiles after RI onset does not change much, and the azimuthally averaged tangential wind never exceeds 25 m s^{-1}. However, the RMW shifts outward, and the winds between 25- and 100-km radius strengthen. Both of these processes reflect the growth of the mesovortex and its transformation into a TC by "consuming" the parent circulation.

Regarding the question of whether a well-defined RMW is a necessary condition for RI, the short answer seems to be *no*, as the sprint mode has no well-defined RMW before RI
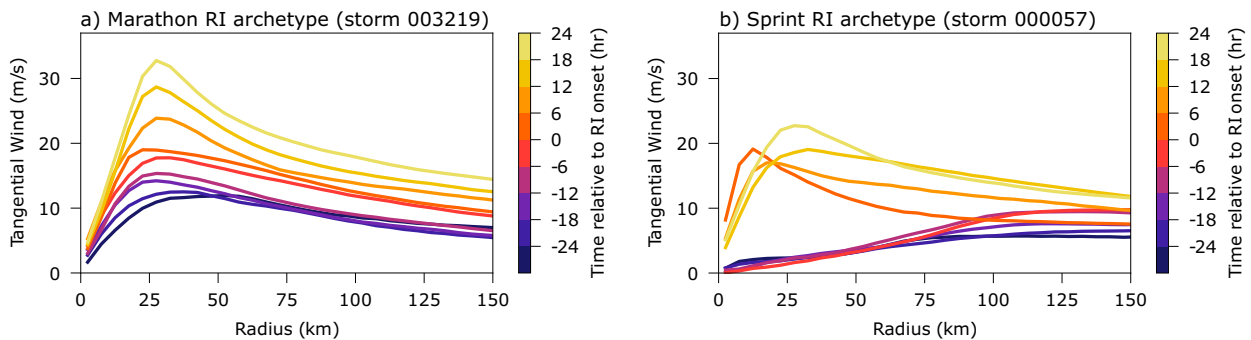
FIG. 7. Radial profiles of azimuthally averaged tangential wind. (a) The marathon mode archetype and (b) the sprint mode archetype. The radial profiles are color-coded by time with respect to RI onset and represent an average over the preceding 6 h (i.e., the profile corresponding to RI onset + 6 h represents the 6-h average from RI onset to RI onset + 6 h).

begins. On the other hand, a RMW does exist before RI in the marathon mode, which suggests that the existence of an RMW is necessary under this RI mode. To support or refute this notion, we also examined the other two marathon cases, and they also show a RMW before RI begins (not shown). However, even with these two more cases, the limited sample size makes generalization difficult.

b. Vertical alignment

When a TC vortex is vertically tilted, vortex alignment refers to the reduction of this tilt, or more specifically, to the reduction of the horizontal distance between the centers of circulation at different levels. The relationship between vertical alignment and RI has been the focus of several studies recently, but there has been no consensus so far on whether or not alignment is necessary before RI can occur. Some studies found that alignment precedes RI and may therefore be a necessary condition (e.g., Rogers et al. 2015; Rios-Berrios et al. 2018), while other studies argue that alignment is merely an incidental process (Chen and Gopalakrishnan 2015; Miyamoto and Nolan 2018).

Usually, vertical misalignment is measured by the distance between the low-level center and the midlevel center (this distance is also referred to as displacement). During the alignment process, the displacement decreases and eventually becomes near-zero when the vortex is vertically erect. Although displacement is an intuitive and quantitative metric, we are not using it in this study because the ill-defined circulation center in the sprint RI case causes problems for the center-finding algorithm, and as a consequence, the displacement values are ambiguous and not representative. Instead, we use sequences of plan-view contour maps of sea level pressure and 500-hPa geopotential height (Fig. 8). This approach may not be quantitative, but it is sufficient to present the differences in vertical alignment between the two RI cases.

The marathon RI case exhibits a classic alignment sequence (Figs. 8a–d). More specifically, the midlevel center is initially (18 h before RI onset) displaced ~100 km to the south of the surface center (Fig. 8a). The vortex tilt does not change much over the following 12 h, and the displacement is more or less the same 6 h before RI onset (Fig. 8b). The tilt then rapidly decreases around the time of RI onset, and by 6 h into the RI period, the surface and midlevel center are vertically aligned (Fig. 8c). The vortex remains aligned during RI (Fig. 8d).

While there is little doubt about the overall evolution from a tilted vortex pre-RI to an aligned vortex, it is difficult to determine the exact order of events: does alignment lead RI onset? Or is it the other way around? Even a plot sequence with 15-min intervals (not shown) does not reveal the answer to this question, and all one can say is that vortex alignment is a fluent, continuous process that takes place around RI onset. Consequently, it is not possible with this dataset to infer whether alignment is necessary for RI to happen or whether alignment is merely a consequence of the beginning RI process.

In the sprint RI case, the alignment process does not follow the canonical alignment process; in fact, the sequence in Figs. 8e–h can hardly be described as "alignment." Rather, the sequence reflects the development of the mesovortex, which was vertically erect from the beginning. The sequence in Figs. 8e–h begins a few hours before the primary intensification burst, at a time when the 500-hPa geopotential field is characterized by a broad depression displaced to the southeast of the surface low (Fig. 8e). A separate, much smaller-scale closed contour near 14°N, 158°E is a manifestation of the convective burst. The 500-hPa circulation tightens up over the following 6 h and migrates closer to the surface center; however, Fig. 8f does not provide evidence for a coherent vortex to have formed at 500 hPa. Another 6 h later, the mesovortex had become apparent as a vertically upright system, characterized by the alignment of a surface and midlevel depression spanning approximately 1° in diameter (~100 km; Fig. 8g). As described before, the mesovortex broadens during the following hours and grows by merging with the parent circulation (Fig. 8h). There is some evidence of a tilt at RI + 18 h, as the geopotential height minimum seems to become displaced to the southeast (Fig. 8h). The development of a new, vertically aligned vortex within the asymmetric convection is consistent with the "downshear reformation" process observed during certain RI cases (Nguyen and Molinari 2015; Chen et al. 2017, 2018; Alvey et al. 2022).

The difference in interplay between lower and upper circulation between the marathon and sprint RI cases (alignment versus development of a new coherent vortex) is an additional piece of evidence in that each RI mode is a manifestation of a

Marathon RI archetype (storm 003219)
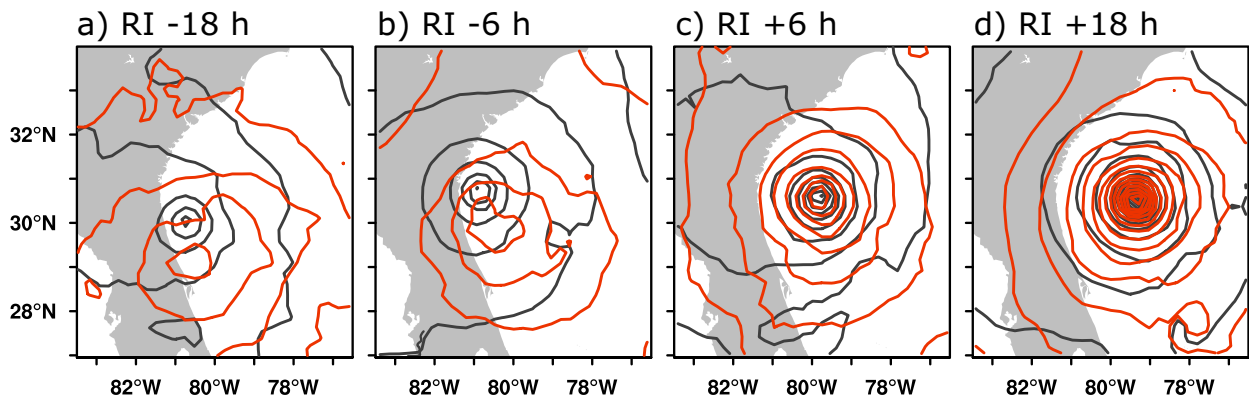
Sprint RI archetype (storm 000057)
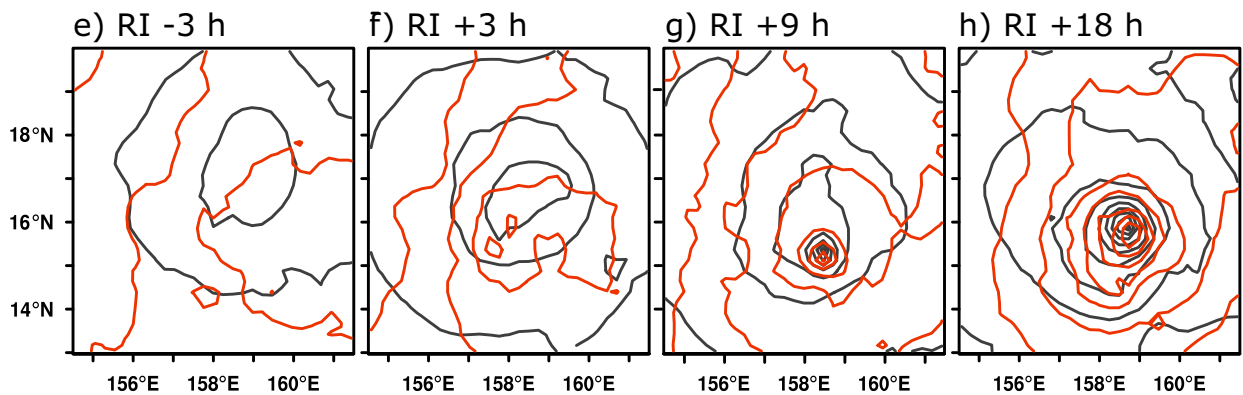
—— sea-level pressure
—— 500-hPa geop. height

FIG. 8. Vertical (mis)alignment as represented by the offset between surface circulation (sea level pressure; black) and midlevel circulation (500-hPa geopotential height; red). (a)–(d) The marathon-mode archetype and (e)–(h) the sprint-mode archetype. Before plotting, the model output has been regridded to a 0.25° grid for noise reduction.

distinct underlying mechanisms. These distinctions beg the question of whether there are also differences in the environment, a topic that will be investigated in the following section.

5. Differences in environmental conditions

The purpose of this section is to document that marathon- and sprint-mode RI occur in distinct environments. To quantify environmental variables, we follow the method of Kaplan and DeMaria (2003) and average these variables within a 200–800-km annulus around the storm center. The variables presented here are deep-layer (850–200 hPa) vertical wind shear and low-level (850–700 hPa) humidity. We use low-level humidity rather than midlevel humidity so we can compare our results with those of Kaplan and DeMaria (2003) and Kaplan et al. (2010) (they did not evaluate midlevel humidity).

The marathon archetype is characterized by a *favorable environment*, that is, in an environment generally conducive for intensification with weak vertical wind shear and relatively

high relative humidity (Fig. 9a). In the 2–3 days before RI begins, the shear is in the 5–10 m s^{-1} range, i.e., of moderate intensity, but decreases to <5 m s^{-1} after RI onset. A 24-h average centered on RI onset yields a value of 4 m s^{-1}, which is generally considered weak shear. There is a noticeable drop in shear magnitude right around RI onset, which could be a manifestation of vertical alignment (the shear calculation does not take tilt into account). Another possibility for the drop in shear is that the outflow, which strengthens as the storm intensifies, "pushes the shear away" (Ryglicki et al. 2019). The shear time series also displays a periodic signal, which looks conspicuously like a diurnal cycle. According to our knowledge, the existence of a diurnal cycle in shear has not explicitly been documented, although the signal could just be a manifestation of the diurnal cycle in the outflow of TCs (Dunion et al. 2019; Ruppert and O'Neill 2019).

The low-level humidity is favorable but not particularly moist. More specifically, humidity is around 60%–70%, with a slight upward trend within the first 4 days of this period
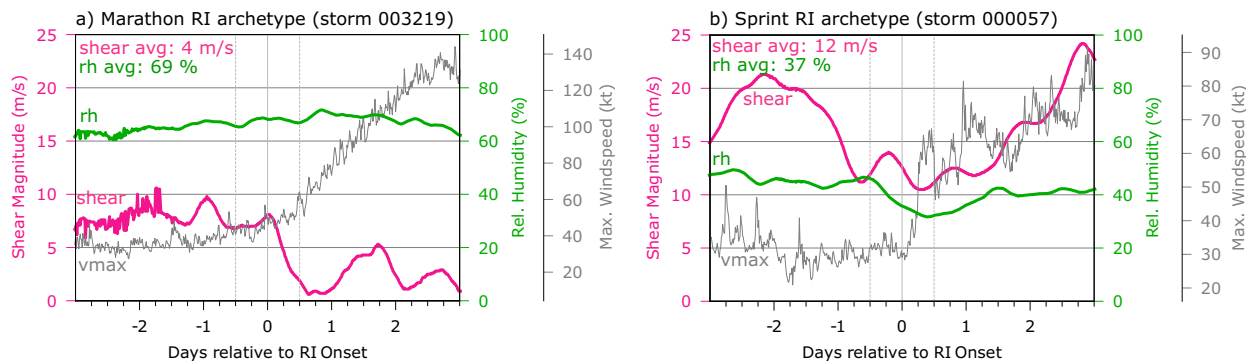
FIG. 9. Time series of deep-layer vertical wind shear magnitude (magenta), low-level relative humidity (green), and v_{max} (gray). (a) The marathon mode archetype and (b) the sprint mode archetype. The dashed vertical lines mark the 24-h period over which the variables are averaged to provide a value representative for RI onset (the values are indicated in the figure).

(Fig. 9a). Averaging over the 24-h period centered on RI onset yields a value of 69%. This value is smaller than the sample mean for all RI cases between 1989 and 2006, which is 74% (Kaplan et al. 2010). The rather moderate value of 69% is likely a consequence of the large annulus and the dry faraway environment (not shown).

In contrast to the favorable environment of the marathon case, the sprint case occurs in a decidedly *unfavorable environment*. In particular, vertical wind shear is strong and relative humidity is low (Fig. 9b). The shear magnitude stays above 10 m s^{-1} throughout the whole six day period displayed in Fig. 9. In fact, shear is above 15 m s^{-1} about half of that time, and only drops below 15 m s^{-1} during 2 days around RI onset. Averaging over a 24-period centered on RI onset yields a shear value of 12 m s^{-1}, which is strong shear and three times as high as in the marathon case. The elevated shear magnitude could explain why the still fairly "young" new vortex in Fig. 8h showed signs of a tilt after the—initially upright—mesovortex had started to broaden. The low-level humidity hovers between 30% and 50% over the 6-day range plotted in Fig. 9b. Averaging over the 24-period centered on RI onset yields a value of 37%, a remarkably low value. In fact, 37% is significantly lower than the mean value for non-RI storms, which is 69% (Kaplan and DeMaria 2003).

Despite these adverse environmental conditions, storm 000057 manages to rapidly intensify. How does it do so? A plausible answer is that RI in this case is intimately tied to the convective bursts. Without the burst, there would be no mesovortex and no RI. The development of convective bursts is not impeded by shear and dry air, in fact, convective bursts seems to occur frequently in sheared storms (Corbosiero and Molinari 2002; Molinari et al. 2012; Hazelton et al. 2017; Alvey et al. 2022). Consequently, the sprint RI mode can be seen as a consequence of unfavorable conditions.

One key ingredient for convective bursts is instability (Molinari et al. 2012). And indeed, the sprint-RI case develops in a background state with high convectively available potential energy (CAPE). Specifically, the western half of the parent circulation draws in ambient air with CAPE values > 3000 J kg^{-1} (Fig. 10b). Located downshear-left of the center of circulation,

the convective burst is sustained by the convergence of conditionally unstable air (Figs. 10b,d). Because of the continuous import of high-CAPE air, the burst endured for 18 h—long enough to ultimately spawn the mesovortex. Downstream of the convective burst, the CAPE is substantially lower (<1000 J kg^{-1}), presumably because downdrafts have transported dry midlevel air to the surface. Because of the weak and broad circulation, the stable air does not circle directly back into the convecting area (which would have cut the convective burst off from its energy supply).

The convective burst and accompanying mesovortex, as depicted in Fig. 5, exhibit a structure that resembles a continental supercell. This similarity is further reinforced by the presence of high CAPE and strong vertical wind shear. Molinari and Vollaro (2010) also recognized the similarity between the convective burst and a supercell in their study of a sheared storm undergoing RI. However, they concluded that the feature was not a supercell due to the distinct distribution of vertical vorticity. Unlike typical continental supercells, where the strongest vorticity occurs in the midlevels, their system had the strongest vorticity in the lower troposphere. Additionally, the mesocyclone in their storm was larger than those observed in tropical cyclone supercells. As a result, they classified the feature as a vortical hot tower (Hendricks et al. 2004). Based on the similarities between the storm analyzed by Molinari and Vollaro (2010) and our storm 000057, we conclude that this classification is also applicable to storm 000057.

For completeness, Figs. 10a and 10c show the CAPE and reflectivity from the marathon case. Even though there are high CAPE values in the environment south of storm 003219, the CAPE values in the core are substantially lower (<2000 J kg^{-1}) than in the sprint case. The reduced CAPE in the core suggests that the intensification here follows a spinup paradigm that does not rely on ambient instability. The high-CAPE environment, however, does seem to feed the outer rainbands.

In summary, the marathon and sprint RI mode occur under very different environmental conditions. The marathon case develops in a favorable, low shear environment, whereas the sprint case develops in an unfavorable, high shear environment. In the sprint case, high CAPE air feeds the long-lived convective burst that spawns the RI-inducing mesovortex. The marathon mode
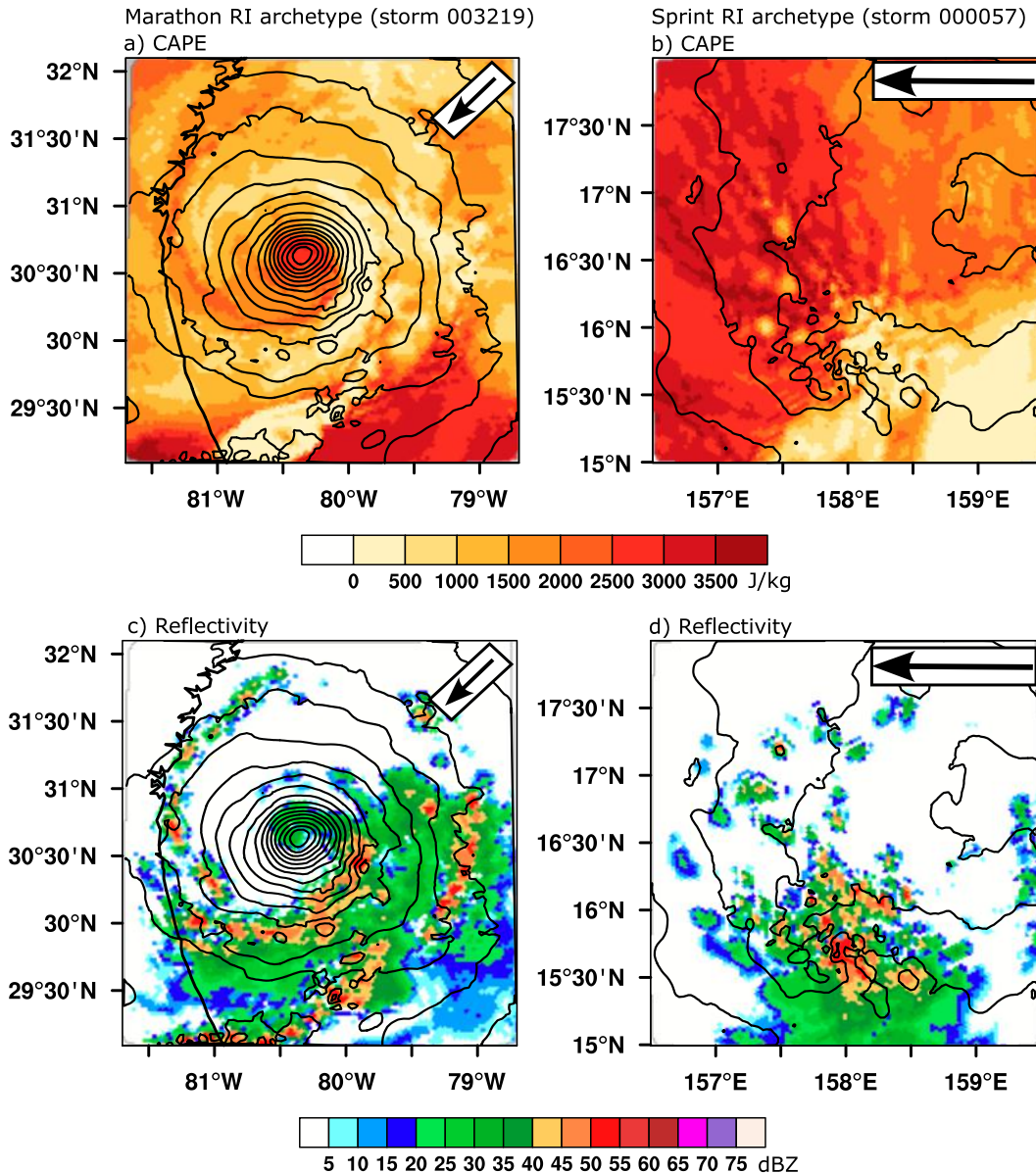
FIG. 10. Snapshots of (a),(b) CAPE and (c),(d) 1-km radar reflectivity, valid at RI onset. Sea level pressure is contoured every 1 hPa. The marathon mode archetype is in (a) and (c) and the sprint mode archetype is in (b) and (d). The arrows in each panel denote the shear direction and magnitude.

seems to rely much less on ambient instability. We also investigated the potential influence of different sea surface temperatures (SST) on RI mode, but we did not observe any consistent patterns. All of the RI cases occurred over water temperatures exceeding 29°C. It is worth noting that sprint RI case 000055 stands out with exceptionally high SST exceeding 31°C (not shown).

6. Identification of marathon and sprint rapid intensification modes in observations

Up until now, our analysis has concentrated solely on a simulation. This prompts us to inquire whether marathon and sprint modes of RI can be discerned through observations. To address this query, we examined the second-generation North Atlantic Hurricane Database (HURDAT2) obtained from the National Hurricane Center (Landsea and Franklin 2013). We implemented specific criteria to classify the RI cases into marathon and sprint modes. We defined storms with at least four consecutive overlapping RI periods as marathon RI cases, while storms with at most two consecutive overlapping RI periods were classified as sprint RI cases. The decision to choose four consecutive RI periods for the marathon mode was based on the observation that the overall RI period for marathon mode RI in Fig. 2 lasts at least one day. The overall results remain reasonably consistent
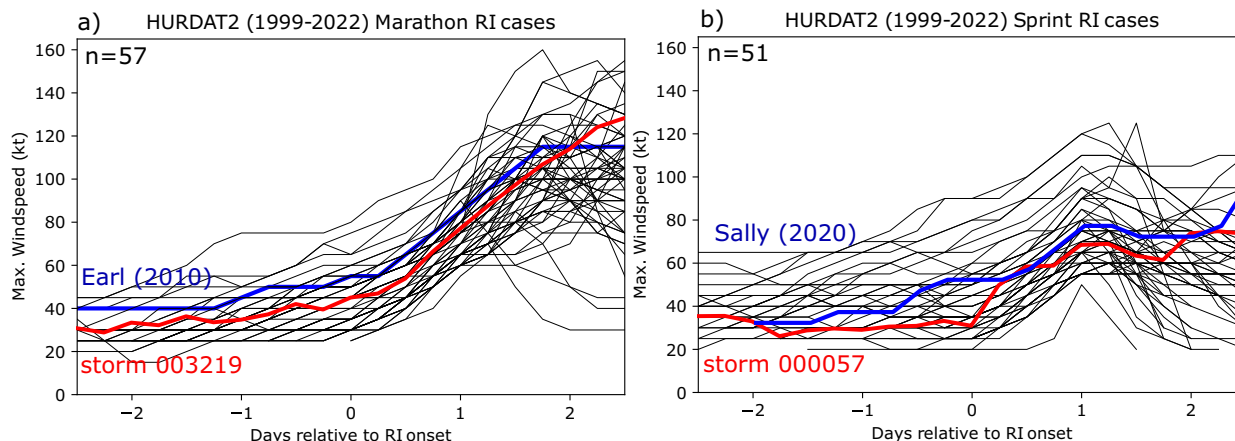
FIG. 11. Classification of (a) marathon and (b) sprint RI cases in the HURDAT2 database (1998–2022). The classification of RI cases was based on the number of consecutive RI periods. A case with four or more consecutive RI periods was classified as a marathon RI case, whereas a case with two or fewer consecutive RI periods was classified as a sprint RI case. Two observational archetypes are highlighted in blue to illustrate the different modes: Hurricane Earl (2010) represents a marathon case, while Hurricane Sally (2020) represents a sprint case. Additionally, the two archetypes identified in the MPAS simulation are highlighted in red.

regardless of the exact duration chosen for the consecutive RI periods. We focus on storms from the 1998 season onward because of better data quality, and we do not allow for double counting. This means that we only classify each storm once, even if, for example, a sprint RI case experienced "marathon RI" at some later point.

After applying the criteria to the 426 storms in the database, we identified 57 marathon RI cases and 51 sprint RI cases (Fig. 11, black lines). When examining the v_{max} time series of the observed storms in each group, we observed a general resemblance to the corresponding time series of the simulated storms. Marathon RI cases exhibit an extended duration of RI, and their intensity peaks approximately 2 days after the onset of RI. On the other hand, sprint cases demonstrate less pronounced intensification, reaching peak intensity around 1 day after the onset of RI, often followed by a period of weakening. Consistent with the findings from our simulation results, marathon cases tend to achieve higher peak intensities (median peak intensity of 115 kt) in comparison to sprint RI cases (median peak intensity of 65 kt).

To provide illustrative examples, we have selected two well-studied storms that serve as observational counterparts to the simulation archetypes. Hurricane Earl of 2010 (Montgomery et al. 2014; Stevenson et al. 2014; Rogers et al. 2015; Chen and Gopalakrishnan 2015; Judt et al. 2016) represents a typical marathon case, demonstrating a gradual intensification prior to entering a 2-day period of RI that ultimately transformed into a powerful major hurricane with a peak intensity of 115 kt (Fig. 11a, blue line). Earl's intensity evolution closely resembles that of storm 003219, the marathon-mode archetype from our simulation (Fig. 11a, red line).

Hurricane Sally of 2020[2] represents a typical sprint case (Fig. 11b, blue line). While Sally's intensity evolution does not precisely match the sprint-RI archetype 000057, detailed

observations from the Tropical Cyclone Rapid Intensification field campaign suggest that Sally can be classified as a sprint-mode RI case (Stone et al. 2023). Key evidence supporting this classification includes the presence of high shear, a convective burst triggering a center reformation, and the subsequent spinup of the new center, resulting in a 20-kt increase in v_{max} within a 12-h timeframe (Stone et al. 2023).

The case of Sally (2020) illustrates that discerning sprint RI cases solely based on intensification rate and RI duration in HURDAT2 is challenging, primarily due to the limitations of the HURDAT2 dataset in capturing the short yet intense periods of rapid intensification that are characteristic of sprint mode cases. To accurately identify sprint RI cases, it is crucial to have access to detailed observations with high temporal and spatial resolution, specifically focusing on the convective structure. Noteworthy studies conducted by Molinari and Vollaro (2010), Nguyen and Molinari (2012), and Stone et al. (2023) exemplify the significance of such detailed observations in understanding sprint RI dynamics.

7. Discussion

The concept of marathon and sprint modes of RI offers a framework for understanding the diverse behaviors of intensifying TCs. The marathon mode aligns with the "canonical" RI mode and corresponds to the RI phase in the three-phase intensification model proposed by Miyamoto and Takemi (2013). By recognizing the equivalence between the marathon mode and the canonical mode of RI, we begin to understand that marathon RI is not only present in nature or complex models but also manifests itself in the most simplified TC models. It serves as the fundamental manifestation of TC spinup. Notably, marathon RI is evident in models as basic as Anthes (1972), Rotunno and Emanuel (1987), Bryan and Rotunno (2009) and Peng et al. (2018). An overwhelming majority of RI studies has focused on unraveling the intricacies of the marathon mode, extensively

---

[2] Although Sally did not strictly meet the "30 kt in 24 h" RI criterion, it did satisfy the "25 kt in 24 h" and "20 kt in 12 h" RI criteria examined in Kaplan et al. (2010, 2015).

examining it through various approaches, including observational analyses (Montgomery et al. 2014; Rogers et al. 2015), real-world simulations (Rogers 2010; Chen and Zhang 2013; Judt and Chen 2016), and idealized simulations (Smith et al. 2009; Miyamoto and Nolan 2018).

The sprint mode of RI can be regarded as noncanonical. In this mode, a convective burst positioned downshear of the center of the parent circulation initiates a center reformation, resulting in the subsequent spinup of a new center, rather than the amplification of the main vortex. Despite its significance, the sprint mode has received little attention in the existing literature. Only a few studies have specifically examined this mode, possibly due to its perceived lack of fascination compared to the well-studied canonical marathon mode RI events (J. Beven 2022, personal communication). Another contributing factor could be the limited representation of the sprint mode in best track data, potentially stemming from the challenge of capturing the short time scales on which sprint mode RI occurs, leading to undersampling issues.

During the direct comparison of archetype storms in sections 4 and 5, we uncovered notable distinctions between the marathon and sprint modes of RI. However, it is crucial to acknowledge that this analysis, which focuses on just two cases, raises questions about the representativeness of these cases. While other storms within each category exhibit similarities to the original archetypes, they also display some variations. These variations emphasize the fact that not all RI events neatly conform to either the marathon or sprint mode, indicating the need to view marathon and sprint RI modes as opposite ends of a spectrum rather than rigid categories. For instance, an RI event may initiate with a convective burst and center reformation, characteristic of the sprint mode, but subsequently transition into a more symmetrical mode of intensification resembling the marathon mode. On the other hand, burst-driven intensification without center reformation can occur when the heating effect projects onto the azimuthal mean, as exemplified by storm 002341 (Fig. 2c), which is more like the marathon mode. These examples highlight the dynamic nature of RI processes and the presence of transitional cases that blur the boundaries between the marathon and sprint modes.

Extreme cases of RI, such as Wilma (2005) and Patricia (2015), may initially appear to be sprint mode cases due to their high intensification rates. However, despite these high intensification rates, these storms are actually classified under the marathon mode. This classification is based on the observation that they undergo a symmetric spinup process, rather than the convective burst and center formation characteristic of the sprint mode. These unique "fast marathons" cases demonstrate the limitations of using intensification rates alone as a criterion for classification. Instead, it is crucial to consider the structural evolution during RI, specifically distinguishing between symmetric and asymmetric modes.

The primary emphasis on intensification rate in Holliday and Thompson (1979) is also the reason why it is difficult to determine whether their type 1 and type 2 RI correspond to our sprint and marathon modes of RI. Drawing definitive conclusions about whether Holliday and Thompson observed the same phenomena as we found in our simulation is challenging due to the absence of vortex structure and underlying process analysis in their study. While there are similarities, such as gradual deepening in type 1 RI (marathon) and abrupt deepening in type 2 RI (sprint), further investigation is required to establish a definitive link.

In a similar vein, the typical and atypical modes of RI in Ryglicki et al. (2018b) share some similarities with the marathon and sprint RI modes, but there are important distinctions to consider. For example, Ryglicki et al. (2018b) did not associate the "atypical RI" mode with the sprint mode's main characteristic, that is, the sequence of events involving convective burst, mesovortex formation, and subsequent new center spinup. Additionally, the study did not explicitly examine the "typical" RI mode, leaving uncertainties about its equivalence to the marathon mode.

8. Summary and Conclusions

We used a 40-day-long global convection-permitting simulation to explore the rapid intensification (RI) of tropical cyclones (TCs). Out of the 23 TCs produced by the simulation, seven experienced RI. Our analysis of these RI cases revealed two distinct modes of intensification: the *marathon RI mode* and the *sprint RI mode*. The marathon mode was characterized by a gradual and sustained intensification period, while the sprint mode exhibited sudden and short-lived bursts of intensification.

To validate our simulation results, we turned to the HURDAT2 database, which contains observational data of TCs. By applying criteria based on the length of the RI period, we confirmed the existence of both marathon and sprint RI modes in the HURDAT2 database as well. This agreement between our simulation and the observational database further supports the validity of our findings.

Examining the vortex structure of the marathon and sprint RI cases in the simulation, we observed clear differences. The marathon mode cases displayed well-defined and symmetric vortices at the onset of RI, whereas the sprint mode cases exhibited asymmetric vortices with poorly defined centers. These structural variations underscored the distinct nature of the two RI modes.

By comparing the archetypes of each mode, we identified unique intensification mechanisms. The marathon archetype involved a symmetric, continuous amplification of the primary vortex, similar to the classic spinup process observed in idealized TCs. On the other hand, the sprint archetype featured an asymmetric intensification process characterized by a chain of discrete events. This chain started with a convective burst that formed in the downshear-left quadrant of a weak and poorly defined parent circulation. The burst spawned a mesovortex, which grew in scale and strengthened while absorbing the parent circulation.

Further analysis revealed contrasting environmental conditions between the two RI modes. The marathon cases occurred in favorable weak-shear environments, consistent with their symmetric intensification and the fact that all marathon RI cases became major hurricanes. In contrast, the sprint RI cases occurred in unfavorable strong-shear environments. While this

may initially seem counterintuitive due to the statistical anticorrelation between high shear and RI, the presence of convective bursts and center reformations explained this phenomenon. Because of the unfavorable environmental conditions, the sprint RI cases were limited in their post-RI peak intensity, with TCs only intensifying from tropical storm to category 1 or 2.

The existence of two RI modes may explain the lack of consensus in certain areas of the literature, such as the role of convective bursts as triggers for RI or the occurrence of RI under strong shear. Moreover, the presence of a shear-driven and asymmetric mode of RI challenges the notion of a single set of necessary conditions for RI. In the end, we hope that this study improves RI predictions by raising awareness that RI in unfavorable conditions, as exemplified by the sprint RI mode, may be more common than commonly thought. It is important to note, however, that our work primarily relied on a single simulation, and further observational, theoretical, and modeling studies are encouraged to validate, refute, or refine our findings.

Data availability statement. We used MPAS version 6.1 to produce the simulation. The model source code is available at https://mpas-dev.github.io. The model output used for this project is stored on the NCAR Supercomputing System and can be made available upon request.

REFERENCES

Alvey, G. R., M. Fischer, P. Reasor, J. Zawislak, and R. Rogers, 2022: Observed processes underlying the favorable vortex repositioning early in the development of Hurricane Dorian (2019). *Mon. Wea. Rev.*, **150**, 193–213, https://doi.org/10.1175/MWR-D-21-0069.1.

Anthes, R. A., 1972: Development of asymmetries in a three-dimensional numerical model of the tropical cyclone. *Mon. Wea. Rev.*, **100**, 461–476, https://doi.org/10.1175/1520-0493(1972)100<0461:DOAIAT>2.3.CO;2.

Becker, T., P. Bechtold, and I. Sandu, 2021: Characteristics of convective precipitation over tropical Africa in storm-resolving global simulations. *Quart. J. Roy. Meteor. Soc.*, **147**, 4388–4407, https://doi.org/10.1002/qj.4185.

Biswas, M. K., D. Stark, and L. Carson, 2018: GFDL vortex tracker users' guide version 3.9a. National Center for Atmospheric Research, Developmental Testbed Center, 35 pp., https://dtcenter.org/sites/default/files/community-code/gfdl/standalone_tracker_UG_v3.9a.pdf.

Bryan, G. H., and R. Rotunno, 2009: The maximum intensity of tropical cyclones in axisymmetric numerical model simulations. *Mon. Wea. Rev.*, **137**, 1770–1789, https://doi.org/10.1175/2008MWR2709.1.

Chen, H., and D.-L. Zhang, 2013: On the rapid intensification of Hurricane Wilma (2005). Part II: Convective bursts and the upper-level warm core. *J. Atmos. Sci.*, **70**, 146–162, https://doi.org/10.1175/JAS-D-12-062.1.

——, and S. G. Gopalakrishnan, 2015: A study on the asymmetric rapid intensification of Hurricane Earl (2010) using the HWRF system. *J. Atmos. Sci.*, **72**, 531–550, https://doi.org/10.1175/JAS-D-14-0097.1.

Chen, X., Y. Wang, K. Zhao, and D. Wu, 2017: A numerical study on rapid intensification of Typhoon Vicente (2012) in the South China Sea. Part I: Verification of simulation, storm-scale evolution, and environmental contribution. *Mon. Wea. Rev.*, **145**, 877–898, https://doi.org/10.1175/MWR-D-16-0147.1.

——, ——, J. Fang, and M. Xue, 2018: A numerical study on rapid intensification of Typhoon Vicente (2012) in the South China Sea. Part II: Roles of inner-core processes. *J. Atmos. Sci.*, **75**, 235–255, https://doi.org/10.1175/JAS-D-17-0129.1.

Computational and Information Systems Laboratory, 2019: Cheyenne: HPE/SGI ICE XA System (Climate Simulation Laboratory). National Center for Atmospheric Research, accessed 25 September 2023, https://doi.org/10.5065/D6RX99HX.

Corbosiero, K. L., and J. Molinari, 2002: The effects of vertical wind shear on the distribution of convection in tropical cyclones. *Mon. Wea. Rev.*, **130**, 2110–2123, https://doi.org/10.1175/1520-0493(2002)130<2110:TEOVWS>2.0.CO;2.

Dunion, J. P., C. D. Thorncroft, and D. S. Nolan, 2019: Tropical cyclone diurnal cycle signals in a hurricane nature run. *Mon. Wea. Rev.*, **147**, 363–388, https://doi.org/10.1175/MWR-D-18-0130.1.

Freitas, S. R., W. M. Putman, N. P. Arnold, D. K. Adams, and G. A. Grell, 2020: Cascading toward a kilometer-scale GCM: Impacts of a scale-aware convection parameterization in the Goddard Earth Observing System GCM. *Geophys. Res. Lett.*, **47**, e2020GL087682, https://doi.org/10.1029/2020GL087682.

Guimond, S. R., G. M. Heymsfield, and F. J. Turk, 2010: Multiscale observations of Hurricane Dennis (2005): The effects of hot towers on rapid intensification. *J. Atmos. Sci.*, **67**, 633–654, https://doi.org/10.1175/2009JAS3119.1.

Hazelton, A. T., R. E. Hart, and R. F. Rogers, 2017: Analyzing simulated convective bursts in two Atlantic hurricanes. Part II: Intensity change due to bursts. *Mon. Wea. Rev.*, **145**, 3095–3117, https://doi.org/10.1175/MWR-D-16-0268.1.

Hendricks, E. A., M. T. Montgomery, and C. Davis, 2004: The role of "vortical" hot towers in the formation of Tropical Cyclone Diana (1984). *J. Atmos. Sci.*, **61**, 1209–1232, https://doi.org/10.1175/1520-0469(2004)061<1209:TROVHT>2.0.CO;2.

Holliday, C. R., and A. H. Thompson, 1979: Climatological characteristics of rapidly intensifying typhoons. *Mon. Wea. Rev.*, **107**, 1022–1034, https://doi.org/10.1175/1520-0493(1979)107<1022:CCORIT>2.0.CO;2.

Hong, S.-Y., J. Choi, E.-C. Chang, H. Park, and Y.-J. Kim, 2008: Lower-tropospheric enhancement of gravity wave drag in a global spectral atmospheric forecast model. *Wea. Forecasting*, **23**, 523–531, https://doi.org/10.1175/2007WAF2007030.1.

Iacono, M. J., J. S. Delamere, E. J. Mlawer, M. W. Shephard, S. A. Clough, and W. D. Collins, 2008: Radiative forcing by long-lived greenhouse gases: Calculations with the AER radiative transfer models. *J. Geophys. Res.*, **113**, D13103, https://doi.org/10.1029/2008JD009944.

Jiang, H., and E. M. Ramirez, 2013: Necessary conditions for tropical cyclone rapid intensification as derived from 11 years of TRMM data. *J. Climate*, **26**, 6459–6470, https://doi.org/10.1175/JCLI-D-12-00432.1.

Judt, F., 2018: Insights into atmospheric predictability through global convection-permitting model simulations. *J. Atmos. Sci.*, **75**, 1477–1497, https://doi.org/10.1175/JAS-D-17-0343.1.

——, and S. S. Chen, 2016: Predictability and dynamics of tropical cyclone rapid intensification deduced from high-resolution stochastic ensembles. *Mon. Wea. Rev.*, **144**, 4395–4420, https://doi.org/10.1175/MWR-D-15-0413.1.

——, and R. Rios-Berrios, 2021: Resolved convection improves the representation of equatorial waves and tropical rainfall variability in a global nonhydrostatic model. *Geophys. Res. Lett.*, **48**, e2021GL093265, https://doi.org/10.1029/2021GL093265.

——, S. S. Chen, and J. Berner, 2016: Predictability of tropical cyclone intensity: Scale-dependent forecast error growth in high-resolution stochastic kinetic-energy backscatter ensembles. *Quart. J. Roy. Meteor. Soc.*, **142**, 43–57, https://doi.org/10.1002/qj.2626.

——, and Coauthors, 2021: Tropical cyclones in global storm-resolving models. *J. Meteor. Soc. Japan*, **99**, 579–602, https://doi.org/10.2151/jmsj.2021-029.

Kaplan, J., and M. DeMaria, 2003: Large-scale characteristics of rapidly intensifying tropical cyclones in the North Atlantic basin. *Wea. Forecasting*, **18**, 1093–1108, https://doi.org/10.1175/1520-0434(2003)018<1093:LCORIT>2.0.CO;2.

——, ——, and J. A. Knaff, 2010: A revised tropical cyclone rapid intensification index for the Atlantic and eastern North Pacific basins. *Wea. Forecasting*, **25**, 220–241, https://doi.org/10.1175/2009WAF2222280.1.

——, and Coauthors, 2015: Evaluating environmental impacts on tropical cyclone rapid intensification predictability utilizing statistical models. *Wea. Forecasting*, **30**, 1374–1396, https://doi.org/10.1175/WAF-D-15-0032.1.

Kieper, M. E., and H. Jiang, 2012: Predicting tropical cyclone rapid intensification using the 37 GHz ring pattern identified from passive microwave measurements. *Geophys. Res. Lett.*, **39**, L13804, https://doi.org/10.1029/2012GL052115.

Landsea, C. W., and J. L. Franklin, 2013: Atlantic hurricane database uncertainty and presentation of a new database format. *Mon. Wea. Rev.*, **141**, 3576–3592, https://doi.org/10.1175/MWR-D-12-00254.1.

Li, Y., Y. Wang, Y. Lin, and X. Wang, 2021: Why does rapid contraction of the radius of maximum wind precede rapid intensification in tropical cyclones? *J. Atmos. Sci.*, **78**, 3441–3453, https://doi.org/10.1175/JAS-D-21-0129.1.

Marchok, T., 2021: Important factors in the tracking of tropical cyclones in operational models. *J. Appl. Meteor. Climatol.*, **60**, 1265–1284, https://doi.org/10.1175/JAMC-D-20-0175.1.

Miyamoto, Y., and T. Takemi, 2013: A transition mechanism for the spontaneous axisymmetric intensification of tropical cyclones. *J. Atmos. Sci.*, **70**, 112–129, https://doi.org/10.1175/JAS-D-11-0285.1.

——, and ——, 2015: A triggering mechanism for rapid intensification of tropical cyclones. *J. Atmos. Sci.*, **72**, 2666–2681, https://doi.org/10.1175/JAS-D-14-0193.1.

——, and D. S. Nolan, 2018: Structural changes preceding rapid intensification in tropical cyclones as shown in a large ensemble of idealized simulations. *J. Atmos. Sci.*, **75**, 555–569, https://doi.org/10.1175/JAS-D-17-0177.1.

Molinari, J., and D. Vollaro, 2010: Rapid intensification of a sheared tropical storm. *Mon. Wea. Rev.*, **138**, 3869–3885, https://doi.org/10.1175/2010MWR3378.1.

——, D. M. Romps, D. Vollaro, and L. Nguyen, 2012: CAPE in tropical cyclones. *J. Atmos. Sci.*, **69**, 2452–2463, https://doi.org/10.1175/JAS-D-11-0254.1.

Montgomery, M. T., J. A. Zhang, and R. K. Smith, 2014: An analysis of the observed low-level structure of rapidly intensifying and mature Hurricane *Earl* (2010). *Quart. J. Roy. Meteor. Soc.*, **140**, 2132–2146, https://doi.org/10.1002/qj.2283.

Nakanishi, M., and H. Niino, 2006: An improved Mellor–Yamada level-3 model: Its numerical stability and application to a regional prediction of advection fog. *Bound.-Layer Meteor.*, **119**, 397–407, https://doi.org/10.1007/s10546-005-9030-8.

——, and ——, 2009: Development of an improved turbulence closure model for the atmospheric boundary layer. *J. Meteor. Soc. Japan*, **87**, 895–912, https://doi.org/10.2151/jmsj.87.895.

Nguyen, L. T., and J. Molinari, 2012: Rapid intensification of a sheared, fast-moving hurricane over the Gulf Stream. *Mon. Wea. Rev.*, **140**, 3361–3378, https://doi.org/10.1175/MWR-D-11-00293.1.

——, and ——, 2015: Simulation of the downshear reformation of a tropical cyclone. *J. Atmos. Sci.*, **72**, 4529–4551, https://doi.org/10.1175/JAS-D-15-0036.1.

——, ——, and D. Thomas, 2014: Evaluation of tropical cyclone center identification methods in numerical models. *Mon. Wea. Rev.*, **142**, 4326–4339, https://doi.org/10.1175/MWR-D-14-00044.1.

Niu, G.-Y., and Coauthors, 2011: The community Noah land surface model with multiparameterization options (Noah-MP): 1. Model description and evaluation with local-scale measurements. *J. Geophys. Res.*, **116**, D12109, https://doi.org/10.1029/2010JD015139.

Peng, K., R. Rotunno, and G. H. Bryan, 2018: Evaluation of a time-dependent model for the intensification of tropical cyclones. *J. Atmos. Sci.*, **75**, 2125–2138, https://doi.org/10.1175/JAS-D-17-0382.1.

Rios-Berrios, R., 2020: Impacts of radiation and cold pools on the intensity and vortex tilt of weak tropical cyclones interacting with vertical wind shear. *J. Atmos. Sci.*, **77**, 669–689, https://doi.org/10.1175/JAS-D-19-0159.1.

——, and R. D. Torn, 2017: Climatological analysis of tropical cyclone intensity changes under moderate vertical wind shear. *Mon. Wea. Rev.*, **145**, 1717–1738, https://doi.org/10.1175/MWR-D-16-0350.1.

——, C. A. Davis, and R. D. Torn, 2018: A hypothesis for the intensification of tropical cyclones under moderate vertical wind shear. *J. Atmos. Sci.*, **75**, 4149–4173, https://doi.org/10.1175/JAS-D-18-0070.1.

Rogers, R. F., 2010: Convective-scale structure and evolution during a high-resolution simulation of tropical cyclone rapid intensification. *J. Atmos. Sci.*, **67**, 44–70, https://doi.org/10.1175/2009JAS3122.1.

——, P. D. Reasor, and J. A. Zhang, 2015: Multiscale structure and evolution of Hurricane Earl (2010) during rapid intensification. *Mon. Wea. Rev.*, **143**, 536–562, https://doi.org/10.1175/MWR-D-14-00175.1.

Rotunno, R., and K. A. Emanuel, 1987: An air–sea interaction theory for tropical cyclones. Part II: Evolutionary study using a nonhydrostatic axisymmetric numerical model. *J. Atmos. Sci.*, **44**, 542–561, https://doi.org/10.1175/1520-0469(1987)044<0542:AAITFT>2.0.CO;2.

Ruppert, J. H., Jr., and M. E. O'Neill, 2019: Diurnal cloud and circulation changes in simulated tropical cyclones. *Geophys. Res. Lett.*, **46**, 502–511, https://doi.org/10.1029/2018GL081302.

Ryglicki, D. R., J. H. Cossuth, D. Hodyss, and J. D. Doyle, 2018a: The unexpected rapid intensification of tropical cyclones in moderate vertical wind shear. Part I: Overview and observations. *Mon. Wea. Rev.*, **146**, 3773–3800, https://doi.org/10.1175/MWR-D-18-0020.1.

——, J. D. Doyle, Y. Jin, D. Hodyss, and J. H. Cossuth, 2018b: The unexpected rapid intensification of tropical cyclones in moderate vertical wind shear. Part II: Vortex tilt. *Mon. Wea. Rev.*, **146**, 3801–3825, https://doi.org/10.1175/MWR-D-18-0021.1.

——, ——, D. Hodyss, J. H. Cossuth, Y. Jin, K. C. Viner, and J. M. Schmidt, 2019: The unexpected rapid intensification of tropical cyclones in moderate vertical wind shear. Part III: Outflow–environment interaction. *Mon. Wea. Rev.*, **147**, 2919–2940, https://doi.org/10.1175/MWR-D-18-0370.1.

Satoh, M., B. Stevens, F. Judt, M. Khairoutdinov, S.-J. Lin, W. M. Putman, and P. Düben, 2019: Global cloud-resolving models. *Curr. Climate Change Rep.*, **5**, 172–184, https://doi.org/10.1007/s40641-019-00131-0.

Skamarock, W. C., J. B. Klemp, M. G. Duda, L. D. Fowler, S.-H. Park, and T. D. Ringler, 2012: A multiscale nonhydrostatic atmospheric model using centroidal Voronoi tesselations and C-grid staggering. *Mon. Wea. Rev.*, **140**, 3090–3105, https://doi.org/10.1175/MWR-D-11-00215.1.

Smith, R. K., M. T. Montgomery, and N. Van Sang, 2009: Tropical cyclone spin-up revisited. *Quart. J. Roy. Meteor. Soc.*, **135**, 1321–1335, https://doi.org/10.1002/qj.428.

Stern, D. P., J. L. Vigh, D. S. Nolan, and F. Zhang, 2015: Revisiting the relationship between eyewall contraction and intensification. *J. Atmos. Sci.*, **72**, 1283–1306, https://doi.org/10.1175/JAS-D-14-0261.1.

Stevens, B., and Coauthors, 2019: DYAMOND: The DYnamics of the atmospheric general circulation modeled on non-hydrostatic domains. *Prog. Earth Planet. Sci.*, **6**, 61, https://doi.org/10.1186/s40645-019-0304-z.

Stevenson, S. N., K. L. Corbosiero, and J. Molinari, 2014: The convective evolution and rapid intensification of Hurricane Earl (2010). *Mon. Wea. Rev.*, **142**, 4364–4380, https://doi.org/10.1175/MWR-D-14-00078.1.

Stone, Ž., G. R. Alvey, J. P. Dunion, M. S. Fischer, D. J. Raymond, R. F. Rogers, S. Sentić, and J. Zawislak, 2023: Thermodynamic contribution to vortex alignment and rapid intensification of Hurricane Sally (2020). *Mon. Wea. Rev.*, **151**, 931–951, https://doi.org/10.1175/MWR-D-22-0201.1.

Thompson, G., P. R. Field, R. M. Rasmussen, and W. D. Hall, 2008: Explicit forecasts of winter precipitation using an improved bulk microphysics scheme. Part II: Implementation of a new snow parameterization. *Mon. Wea. Rev.*, **136**, 5095–5115, https://doi.org/10.1175/2008MWR2387.1.

Wang, C., J. Fang, and Y. Ma, 2022: Structural changes preceding the rapid intensification of Typhoon Lekima (2019) under moderate vertical wind shear. *J. Geophys. Res. Atmos.*, **127**, e2022JD036544, https://doi.org/10.1029/2022JD036544.

Wang, H., and Y. Wang, 2014: A numerical study of Typhoon Megi (2010). Part I: Rapid intensification. *Mon. Wea. Rev.*, **142**, 29–48, https://doi.org/10.1175/MWR-D-13-00070.1.

Wang, W., 2022: Forecasting convection with a "scale-aware" Tiedtke cumulus parameterization scheme at kilometer scales. *Wea. Forecasting*, **37**, 1491–1507, https://doi.org/10.1175/WAF-D-21-0179.1.

Wu, Q., and Z. Ruan, 2021: Rapid contraction of the radius of maximum tangential wind and rapid intensification of a tropical cyclone. *J. Geophys. Res. Atmos.*, **126**, e2020JD033681, https://doi.org/10.1029/2020JD033681.

Xu, K.-M., and D. A. Randall, 1996: A semiempirical cloudiness parameterization for use in climate models. *J. Atmos. Sci.*, **53**, 3084–3102, https://doi.org/10.1175/1520-0469(1996)053<3084:ASCPFU>2.0.CO;2.

Yang, Z.-L., and Coauthors, 2011: The community Noah land surface model with multiparameterization options (Noah-MP): 2. Evaluation over global river basins. *J. Geophys. Res.*, **116**, D12110, https://doi.org/10.1029/2010JD015140.

Zhang, F., Y. Qiang Sun, L. Magnusson, R. Buizza, S.-J. Lin, J.-H. Chen, and K. Emanuel, 2019: What is the predictability limit of midlatitude weather? *J. Atmos. Sci.*, **76**, 1077–1091, https://doi.org/10.1175/JAS-D-18-0269.1.